TECHNICAL ARTICLE



Tailoring the Properties of a Ni-Based Superalloy via Modification of the Forging Process: an ICME Approach to Fatigue Performance

Martin Detrois 1 · John Rotella 2 · Mark Hardy 3 · Sammy Tin 4 · Michael D. Sangid 2,5 p

Received: 28 August 2017 / Accepted: 18 October 2017 / Published online: 1 November 2017 © The Minerals, Metals & Materials Society 2017

Abstract Traditionally, material design and property modifications are usually associated with compositional changes. Yet, subtle changes in the manufacturing process parameters can also have a dramatic effect on the resulting material properties. In this work, an integrated computational materials engineering (ICME) framework is adopted to tailor the fatigue performance of a Ni-based superalloy, RR1000. An existing fatigue model is used to identify microstructural features that promote enhanced fatigue life, namely a uniform, fine grain size distribution, random orientation, a distinct grain boundary distribution (specifically high twin boundary density and limited low-angle grain boundaries). A deformation mechanism map and process models for grain boundary engineering of RR1000 are used to identify the optimal thermo-mechanical processing parameters to realize these desirable microstructural features. For validation, small-scale forgings of RR1000 were produced and heat-treated to attain fine grain and coarse grain microstructures that represent the conventionally processed and grain boundary engineered (GBE) conditions, respectively. For each of the four microstructural variants of RR1000, the twin density and grain size were characterized

and were in agreement with the desired microstructural attributes. In order to validate the deformation mechanisms and fatigue behavior of the material, high-resolution digital image correlation was performed to generate strain maps relative to the microstructural features. The high density of twin boundaries was confirmed to inhibit the length of slip bands, which is directly attributed to extended fatigue life. Thus, this study demonstrated the successful role of models, both process and performance, in the design and manufacture of Ni-based superalloy disk forgings.

Keywords Grain boundary engineering $\cdot \Sigma 3 \cdot \text{Twin} \cdot \text{Fatigue} \cdot \text{Strain} \cdot \text{Modeling}$

Introduction

Due to their characteristic anomalous strengthening behavior, Ni-based superalloys are well suited for use as structural components in the hot sections of advanced gas turbine engines [1]. Since the 1950s, many decades of engineering advances have contributed to optimizing their thermo-mechanical properties, such as their resistance to creep, fatigue, and corrosion at elevated temperatures [2]. Much of the unique characteristics of Ni-based superalloys can be attributed to their γ - γ' microstructure, where ordered Ni₃Al γ' precipitates that possess a L1₂ crystal structure are embedded within a disordered Ni facecentered cubic (FCC) y matrix. Thus, the excellent hightemperature strength and creep resistance can be attributed to potent levels of precipitate strengthening that restrict dislocation motion during plastic deformation [3]. In many instances, the properties of these alloys can be further tailored or engineered by modifying the grain boundary structure or character distribution [4–6]. For example, the fatigue properties of high strength, polycrystalline Ni-based superalloys are highly



Michael D. Sangid msangid@purdue.edu

ORISE, National Energy Technology Laboratory, 1450 Queen Ave. SW, Albany, OR 97321, USA

School of Materials Engineering, Purdue University, 701 W. Stadium Ave., West Lafayette, IN 47907, USA

Rolls-Royce plc, Derby DE24 8BJ, UK

Illinois Institute of Technology, 10 W. 32nd Street, Chicago, IL 60616, USA

School of Aeronautics and Astronautics, Purdue University, 701 W. Stadium Ave., West Lafayette, IN 47907, USA

sensitive to both the grain size and grain boundary character distributions [7–9]. In recent years, demand for increasing performance requirements and operating temperatures for advanced turbine engines has pushed the capabilities of existing polycrystalline Ni-based superalloys toward their limitations. As a result, an improved understanding of the dependence of crack initiation and growth mechanisms on grain boundary character distributions can potentially contribute to the identification and development of optimized microstructures that can effectively extend the capabilities of the material.

Polycrystalline materials possess a grain boundary network, where each individual boundary between neighboring grains corresponds to a specific misorientation angle relative to the orientation of the corresponding lattices. The resulting character of the grain boundary segment greatly influences both the physical and mechanical properties of a material [10–12]. Depending on the relative orientations of the highangle grain boundaries (HAGBs), the coherency of the boundary between the individual grains with their neighbors may vary significantly [13]. The coincident site lattice (CSL) is often used to quantify the degree of coherency along grain boundaries and describes the number of positions in the respective lattices of neighbor grains where lattice points coincide [14]. The degree of coincidence and structure of the coincidence sites can be described by the Σ value, used as a parameter defining CSL boundaries. Boundaries with few coincident sites, e.g., low-CSL boundaries typically with $\Sigma > 29$, tend to contain large concentrations of crystalline defects and vacancies that serve to both weaken the interface and promote diffusive mechanisms at elevated temperatures [13]. Since grain boundary diffusion and sliding are accelerated along these boundaries, this leads to environmental degradation and poor resistance to creep deformation. On the other hand, adjacent or neighboring grains that exhibit high-CSL boundaries, or Σ < 29, have relatively coherent interfaces that contain fewer crystalline defects that contribute to weakening the boundaries. Moreover, since there are comparatively fewer vacancies and defects along low- Σ interfaces, the mechanisms by which diffusion and mass transport occur along the interfaces also become more sluggish. Among low- Σ boundaries, twin boundaries, $\Sigma 9$ and $\Sigma 27$, to name a few, are referred to as special grain boundaries. 1 These interfaces typically show lower grain boundary energies compared to those of low-CSL boundaries and HAGBs [15, 16]. Coherent twin or Σ 3 boundaries are the most prevalent type of special grain boundaries [17] and possess the lowest grain boundary energy [16]. Therefore, they are highly desirable features for breaking up the connectivity of the random grain boundary network.

¹ It is noted that a complete description of the GB requires five degrees of freedom (three for orientation and two for the GB normal). While the GB networks discussed herein do not represent a unique description of each GB, they are sufficient to demonstrate correlations for the resulting material performance.



Various grain boundary engineering approaches have been investigated in recent years as increasing the density of coherent twin boundaries has been shown to be an effective strengthening mechanism in polycrystalline materials, while simultaneously maintaining a high degree of ductility [18]. When applied to Ni-based superalloys, grain boundary engineering has been shown to increase resistance to fatigue crack growth and extend the high cycle fatigue life [19, 20]. When either a large grain or a cluster of grains within a polycrystalline microstructure are favorably oriented for planar slip, cyclic deformation conditions may lead to the formation of persistent slip bands that effectively serve as precursors for nucleation of fatigue cracks [21]. Since the length of the persistent slip bands determine the likelihood of crack nucleation, populating the microstructure with a high density of $\Sigma 3$ twin or high-CSL boundaries will serve to inhibit slip transmission across these boundaries and effectively limit their overall length [21]. Since the length of persistent slip bands are bounded by these $\Sigma 3$ boundaries, the eventual nucleation of fatigue cracks will likely occur along these boundaries and is consistent with observations in both pure metals [22–24] and alloys [21, 25, 26]. Furthermore, the tendency of cracks to form along twin boundaries [26-30] can also be attributed to the high degree of elastic strain anisotropy [31, 32] that exists across these boundaries and induce stress concentrations that lead to strain localization.

In recent years, microstructure explicit fatigue models for polycrystalline Ni-based superalloys have been developed [33–40] that confirm strain localization around microstructural features, primarily at twin boundaries, prior to nucleation of fatigue cracks. For this particular study, the finite elementbased crystal plasticity model was used to inform the design of microstructures and identify desirable meso-scale grain boundary character distributions that could be varied to enhance the fatigue performance of a commercially available Nibased superalloy RR1000. Following which, innovative hot deformation based grain boundary engineering techniques were used to systematically vary the grain boundary character distributions in small-scale forgings of RR1000. Detailed strain mapping and microstructural characterization of the forged alloy were used to validate the effectiveness of grain boundary engineering on fatigue crack nucleation behavior.

Design for Fatigue Enhancement

A fatigue model was used to inform the design of the microstructure of an existing Ni-based superalloy, RR1000, in order to enhance the fatigue performance. In this material, one of the primary mechanisms that govern the fatigue life at low temperatures is based on failure due to persistent slip bands (PSBs), in which strain is localized within the microstructure. Tanaka and Mura modeled the energy of a PSB [41], which

has been extended to account for the role of grain boundaries by Sangid et al. [42] and implemented into a polycrystalline formulation [43]. The material of interest, RR1000, has been characterized via electron backscatter diffraction (EBSD), and the microstructural attributes have been used to create a virtual instantiation of the material. A statistically equivalent microstructure was created that matches the distribution of grain size and grain boundary content (including density of twins), possesses a random texture, and is sufficiently large to match the cyclic strength properties of the material (in terms of yield, hardening behavior, and maximum stress during strain controlled cyclic loading) [40]. For more details of the microstructure generation and meshing, please refer to reference [40]. In order to obtain the micromechanical fields relative to the microstructure, a crystal plasticity model was implemented.

The flow rule describing the shear strain rate, $\dot{\gamma}^{\alpha}$, on an individual slip system, α is governed by the following:

$$\dot{\gamma}^{\alpha} = \dot{\gamma}_{o} \left| \frac{\tau^{\alpha} - \chi^{\alpha}}{g^{\alpha}} \right|^{m} sgn(\tau^{\alpha} - \chi^{\alpha}) \tag{1}$$

where γ_0 is the reference shearing rate, m is the strain rate sensitivity, τ^{α} is the corresponding shear stress on the slip system α , g^{α} is the critical resolved shear stress of the slip system α , and χ^{α} is the back stress along slip system α . The critical resolved shear stress on each slip system is updated, g^{α} , to account for isotropic hardening.

$$\dot{g}^{\alpha} = H \sum_{\beta=1}^{N} q^{\alpha\beta} \left| \dot{\gamma}^{\beta} \right| - Rg^{\alpha} \sum_{\beta=1}^{N} \left| \dot{\gamma}^{\beta} \right|$$
 (2)

where H and R are the direct hardening and dynamic recovery coefficients and the latent hardening $q^{\alpha\beta}$ represents the interactions between slip systems, such that the coefficient is 1 for self-hardening ($\alpha = \beta$) and 1.2 for latent-hardening ($\alpha \neq \beta$). The back stress evolution, $\dot{\chi}^{\alpha}$, is expressed as an Armstrong–Frederick type equation [44]:

$$\dot{\chi}^{\alpha} = c_1 \dot{\gamma}^{\alpha} - c_2 \chi^{\alpha} |\dot{\gamma}^{\alpha}| \tag{3}$$

The non-linear kinematic hardening is expressed by Eq. 3, where c_1 and c_2 are the direct hardening and dynamic recovery coefficients, respectively. The output of the crystal plasticity model provides the stresses and strains along each slip system within the microstructure. In each grain, it is assumed that a PSB forms across the centroid of the grain along the slip system that contains the highest shear stress. The energy of the PSB is expressed as follows:

$$E_{PSB} = \Sigma_{i} \bigg[\bigg\{ f \big]_{0}^{L} \gamma_{APB} dL + (1-f) \big]_{0}^{L} \gamma_{SFE} dL \bigg\} + \bigg\{ \tilde{\tau}^{\alpha} \mathit{bL} \bigg\} + \bigg\{ E_{GB}^{\gamma} \mathit{n}_{\mathit{ext}} \mathsf{b} \bigg\} \bigg] \partial X_{i} \qquad \left(4 \right)$$

where ∂X_i is the incremental slip within the PSB with an associated energy barrier expressed as three terms. The first term represents the energy to form the PSB, where f is the volume

fraction of the γ' precipitates phase, γ_{SFE} is the stacking fault energy (SFE) of the γ phase, γ_{APB} , is the anti-phase boundary energy (APB) of the γ' precipitate, and L is the length of the PSB traversing throughout the grain. The SFE and APB represent the energy barriers to shear the γ matrix and γ' precipitate, respectively, in forming the PSB. In this model construction, the SFE and APB values are calculated using molecular dynamic simulations based on the normal stress on the slip plane as stipulated from the crystal plasticity model.

Next, the second term in Eq. 4 represents the energy associated with the slip system level stress within the PSB, $\tilde{\tau}^{\alpha}$, based on the dislocation pile-up stress inside the PSB [45] with a Taylor type hardening term [46] and the change in shear stress on the slip system during a loading cycle as calculated from the crystal plasticity simulation, $\Delta \tau^{\alpha}$. Further, b is the Burgers vector. The final term in Eq. 4 represents interaction energy between the PSB and GB, where E_{GB}^{γ} is the transmission energy for a dislocation to penetrate through a specific grain boundary type, as detailed in reference [47]. Also, n_{ext} is the size of the extrusion or step that forms at the grain boundary, based on an expression of the form given by Mughrabi et al. [48, 49], such that

$$n_{ext} = \dot{\gamma}^{\alpha} b \tilde{L} \frac{\tilde{\tau}^{\alpha}}{\tau_{s}} \sqrt{N}$$
 (5)

In Eq 5, \tilde{L} is the length of the PSB normalized by the average grain size in the material, N is the number of loading cycles, and τ_s is the modified Stroh's stress [50], accounting for the energy associated with the specific type of GB.

$$\tau_s = \left\{ \frac{\pi E_{GB}^{\gamma} \mu}{2(1-\nu)L} \right\}^{\frac{1}{2}} \tag{6}$$

Moreover, μ is the shear modulus, ν is the Poisson's ratio.

The PSBs are observed to transverse through low-angle grain boundaries (LAGBs) with misorientations less than 15° [21, 51], thereby resulting in an overall PSB length that can stretch over multiple connected grains [21, 52]. Failure (e.g., fatigue crack initiation) would occur when the energy of the PSB would attain its stable, minimum value, that is as follows:

$$\frac{\partial E_{PSB}}{\partial X_i} = 0 \quad and \quad \frac{\partial^2 E_{PSB}}{\partial^2 X_i} > 0 \tag{7}$$

Each PSB in the virtual polycrystal was monitored and the critical PSB is defined as the PSB that is the first to reach its stable value. A detailed sensitivity analysis, uncertainty quantification, and uncertainty propagation study for the fatigue model are available in ref. [53].

Next, in order to use the fatigue model to inform the microstructural design of the alloy, we studied the effect of the



grain boundaries on the fatigue behavior. For the results discussed in reference [40], the energy balance for a critical PSB was modified to probe the role of the adjacent grain boundary on the fatigue life. As shown in Fig. 1, a single grain (of diameter 9 µm) was selected and the GB energy around the PSB was varied from a lower limit of 60 mJ/m² (corresponding to a coherent twin) to an upper limit of 932 mJ/m² (corresponding to a HAGB, specifically a 38.94° tilt around the [110]) [54], keeping all the other microstructure parameters within the fatigue model constant. The analysis was repeated for a grain cluster (PSB of length 20 µm that spans across a LAGB). A GB with a lower energy is less likely to nucleate dislocations and provides a stronger barrier for dislocation transmission (for similar type of dislocations and stress conditions). Therefore, it is less likely to form a PSB or resulting extrusions at the GBs, thereby prolonging failure and a longer fatigue life. For this reason, we adopted the strategy of increasing the density of low energy grain boundaries, e.g., coherent twin boundaries, via grain boundary engineering.

Grain Boundary Engineering

Typical grain boundary engineering (GBE) processes known today were first introduced in the mid-1980s and consist of cold rolling/working at strains ranging from 5 to 20% followed by a short annealing time at high temperature, in order to promote the formation of annealing twins [55, 56]. Subsequent iterations of deformation/anneal are often performed in order to obtain a sufficient fraction of twin boundaries [57]. The iterations also allow for the interaction of $\Sigma 3^n$ (n = 1,2,3) boundaries to induce multiple twinning, the formation of incoherent twins, or triple junctions. From a commercial manufacturing perspective, room temperature deformation of high-strength Ni-based superalloys, such as RR1000, is impractical as these materials can withstand

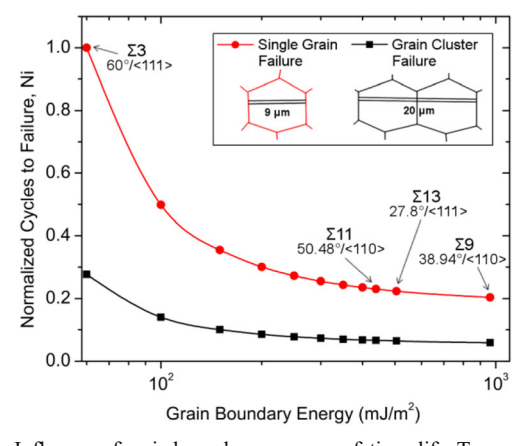
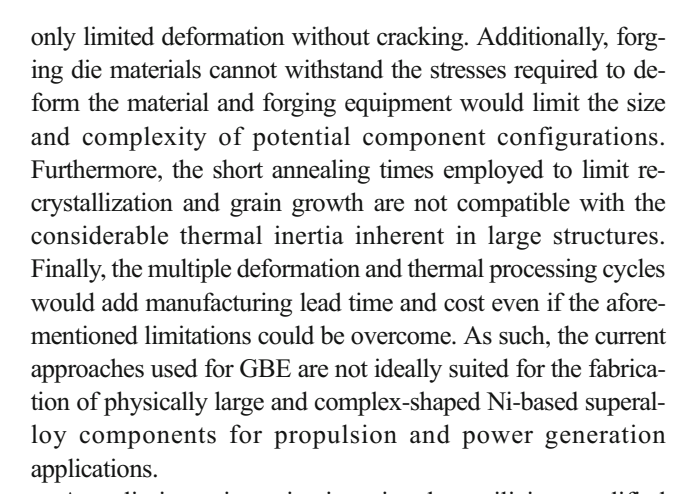


Fig. 1 Influence of grain boundary energy on fatigue life. Two examples are shown based on simulation results, where a PSB is contained within a single grain (red curve) and a PSB traverses a LAGB forming a grain cluster (black curve)



A preliminary investigation aimed at utilizing modified isothermal forging techniques was performed to aid in the understanding of how deformation parameters affect the formation of coherent twin boundaries [58-62]. It was concluded that modest changes in the isothermal deformation parameters are sufficient to control the amount of residual strain energy stored in the deformed material [58]. During deformation, strain energy in the form of dislocations is stored within the grains. Subsequent annealing triggers the formation of coherent twin boundaries via strain-induced grain boundary migration (SIBM). From the experimental results, constitutive models commonly used for describing the formation of twin boundaries in polycrystalline materials were used to quantify the density and length fraction of $\Sigma 3$ boundaries as a function of the grain size [63]. The models were further modified to account for the influence of deformation based on the magnitude of strain energy [59] similar to the work of Li et al. on cold rolling [64, 65]. The resulting density and length fraction of Σ 3 boundaries as a function of the average grain size are expressed in Eqs. 8 and 9 where d is the density of Σ 3 boundaries, k_n (n = 1 to 5) are the constants independent of temperature, E_s is the stored strain energy, D is the grain size, D_{ascp} is the grain size in the deformed condition prior to annealing, $LF_{\Sigma 3}$ is the length fraction of $\Sigma 3$ boundaries, LF^* is the fraction limit.

$$d = k_1 \frac{(1 + k_2 E_s)}{D} \ln \left(\frac{D}{k_3 D_{ascp}} \right) \tag{8}$$

$$LF_{\Sigma 3} = LF^*(1 + k_4 E_s) \left\{ 1 - \exp\left(-\frac{D}{k_5 D_{ascp}}\right) \right\}$$
 (9)

The equations were plotted for deformation parameters leading to negligible amounts and high densities of intragranular misorientations in Fig. 2. For each condition, the density of $\Sigma 3$ boundaries was found to decrease with increasing grain size due to the loss of the twin boundaries in the grains being consumed during grain growth. Conversely, the length fraction of $\Sigma 3$ boundaries increased with increasing grain size due to the



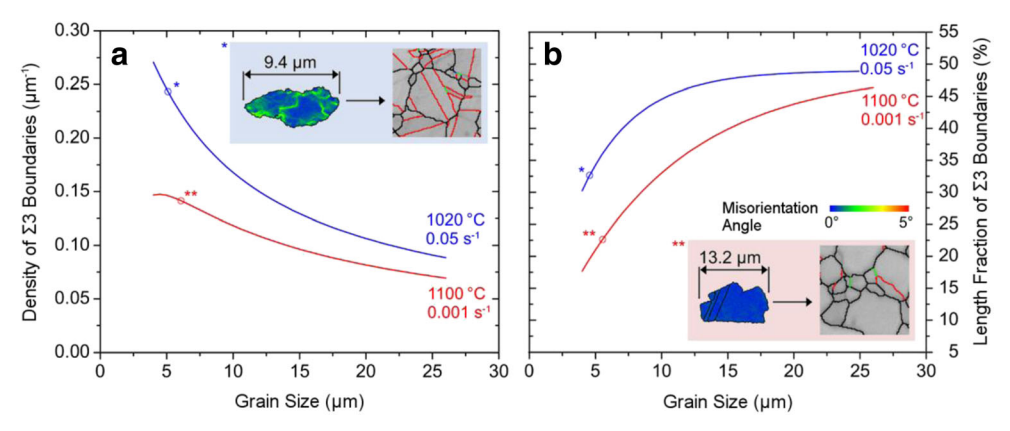


Fig. 2 a Density and b length fraction of $\Sigma 3$ boundaries as a function of varying grain size from annealing heat treatments for two different deformation conditions. Modeled for RR1000 from experimental data and adapted from Ref. [59]. The insets represent the

transformation from deformed grain following forging (using intragranular misorientation maps) to final microstructure following annealing (with $\Sigma 3$ boundaries in red, $\Sigma 9$ in green, $\Sigma 27$ in blue, and random HAGBs in black)

extension of the grain boundary network that decreases the length of the random HAGBs, while the twin boundaries extend across the growing grains. Overall, higher densities and length fractions of $\Sigma 3$ boundaries are shown across the range of grain sizes following annealing of structures that contain the high density of intragranular misorientations, inset of Fig. 2a. Consequently, these results support the notion that the isothermal forging parameters can be optimized and used to control the grain boundary character distribution of polycrystalline Nibased superalloys.

A deformation mechanism map was generated for RR1000 using small-scale cylindrical samples for isothermal compression testing on a Gleeble system to simulate isothermal forging, Fig. 3 [58]. Decreasing the deformation temperature and increasing the strain rate resulted in an increase in the magnitude of intragranular misorientation and the maximum flow stresses measured during deformation. Two regions were identified in the map of Fig. 3 using the initiation of strain hardening. In the superplastic flow region, the higher deformation temperatures and slower strain rates did not induce the storage of sufficient levels of strain energy as grain rotation and sliding occurs during deformation. Consequently, those conditions were not conducive to the formation of annealing twins. Conversely, when dislocation-based plasticity mechanisms are operative during deformation at lower temperatures and higher strain rates, the generation of geometrically necessary dislocations (GNDs) enables storage of strain energy that can promote SIBM during subsequent annealing. Thus, selecting deformation parameters for RR1000 that correspond to this region of the deformation mechanism map is favorable for promoting the formation of annealing twins.

Conventional isothermal forging of RR1000 utilizes deformation parameters that fall within the superplastic flow region of the deformation mechanism map of Fig. 3. In order to increase the density of twin boundaries in the microstructure of the material following deformation and annealing, the deformation

parameters were modified such that the dominant mechanism for accommodating strain was shifted toward the regime where dislocation-based plasticity becomes operative.

Forging

Small-scale forging trials of RR1000 were performed on cylinders measuring 38 mm in diameter and 38 mm length extracted from a consolidated RR1000 billet using electrical discharge machining (EDM). The cylinders were sent to ATI Ladish for isothermal forging using two sets of forging parameters. First, the baseline microstructure was produced by forging the material using a set of deformation parameters typical for isothermal forging with a temperature of 1100 °C and a strain rate of 0.003 s⁻¹. Secondly, a GBE microstructure was produced using a deformation temperature of 1020 °C and a strain rate of 0.05 s⁻¹. Following compression to 0.75 strain, the forged pancakes measured \sim 10 mm in height and \sim 79 mm in diameter. EBSD maps

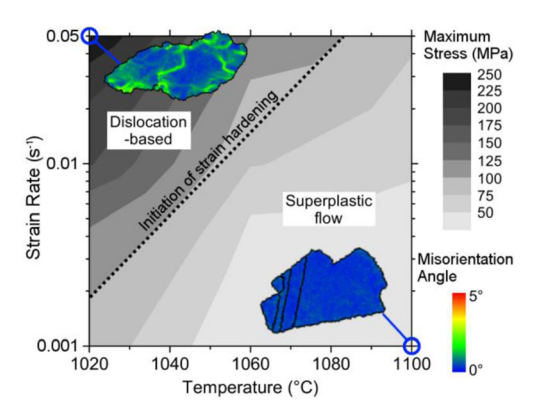
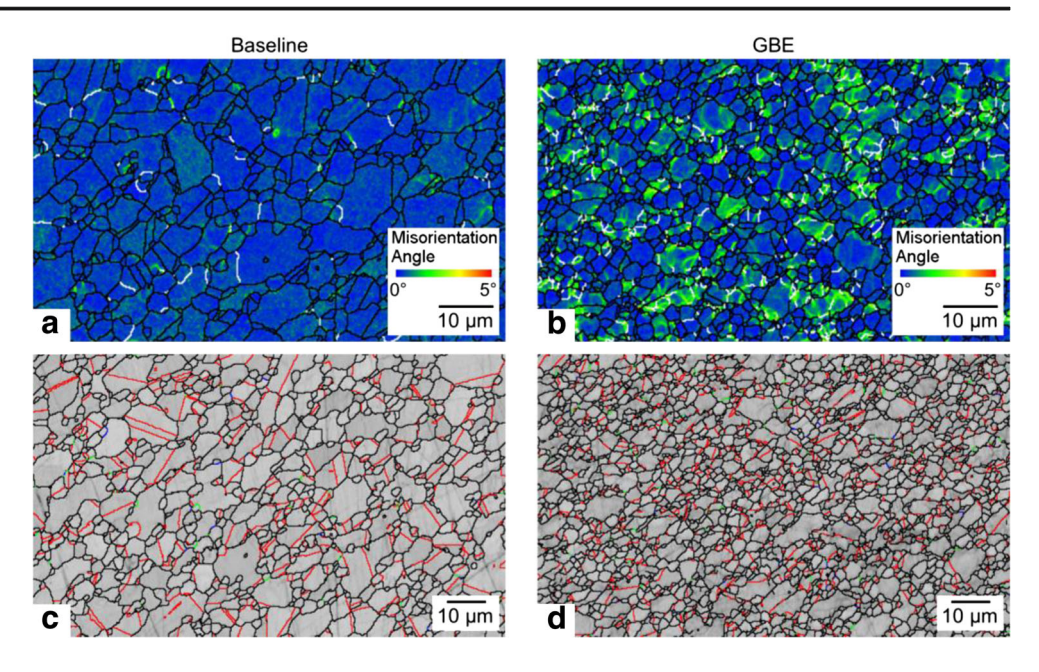


Fig. 3 Deformation mechanism map for RR1000 showing the maximum stress as a function of the deformation temperature and strain rate with intragranular misorientation maps for the samples deformed at $1020 \,^{\circ}\text{C}-0.05 \, \text{s}^{-1}$ and $1100 \,^{\circ}\text{C}-0.001 \, \text{s}^{-1}$. The inset shows an example grain with intragranular lattice misorientation indicated. Adapted from Ref. [58]



Fig. 4 a, b Intragranular misorientation and c, d grain boundary maps for the asdeformed a, c baseline and b, d GBE forged billets. The $\Sigma 3$ boundaries are represented in red, $\Sigma 9$ in green, $\Sigma 27$ in blue, and random HAGBs (misorientation angle $\geq 15^{\circ}$) in black. The LAGBs ($5^{\circ} \leq$ misorientation angle $< 15^{\circ}$) are represented in white in the intragranular misorientation maps



of the forged baseline and GBE material are shown in Fig. 4. The criterion used to constitute a grain boundary was based on a 5° misorientation between neighboring points. The EBSD data was gathered with step sizes 0.5 and 1 μ m for the fine and coarse grain specimens, respectively. Consistent with the deformation mechanism map of Fig. 3, the baseline microstructure presented negligible levels of GNDs, Fig. 3a, while the GBE material exhibited a significant degree of intragranular lattice misorientation, Fig. 3b.

Following deformation, the average grain size was smaller in the GBE condition at 2.6 μm compared to 4.1 μm in the baseline material. Similarly, the length fraction of $\Sigma 3$ boundaries was lower in the GBE condition at 13% compared to 21% in the baseline forging. Additional details on the calculation of the density and length fraction of $\Sigma 3$ boundaries as well as the generation of intragranular misorientation maps can be found in Ref. [60].

The forgings were cut into halves and subject to either a subsolvus or super-solvus heat treatment. The sub-solvus heat treatment was performed at 1115 °C for 4 h, while the super-solvus heat treatment was performed at 1170 °C for 4 h following 4 h at 1115 °C. For all cases, a controlled cooling rate of 1 °C/s was maintained from the heat treatment temperature. During supersolvus heat treatment, above 1140 °C, the dissolution of the primary γ' precipitates originally pining the grain boundaries allows for grain growth [66]. Thus, the sub-solvus condition is referred to as fine grain (FG) and the super-solvus annealing corresponds to coarse grain (CG) microstructures. The processing conditions for the four variants of RR1000 are summarized in Table 1. The grain boundary character distributions of the heattreated forgings are characterized in Figs. 5 and 6. Most Σ 3 boundaries were present as coherent twin boundaries elongated throughout the grains. The FG, conventionally forged material (referred to as the baseline condition), exhibited densities and length fractions of $\Sigma 3$ boundaries of 0.14 μm^{-1} and 25%, respectively, where the density was defined as the length of the $\Sigma 3$ boundaries taken from the EBSD maps divided by the map area [60]. The values are averages over 8 stitched regions which resulted in total scanned areas of $\sim 200 \times 248 \ \mu m^2$. Significantly higher values were measured in the FG GBE forging at 0.27 µm⁻¹ and 39%, respectively. Similarly, higher values were also obtained in the CG microstructure of the GBE-forged material, of $0.06 \, \mu \text{m}^{-1}$ and 46% compared to $0.04 \, \mu \text{m}^{-1}$ and 45% in the baseline material. However, the differences in the values of density and length fraction of $\Sigma 3$ boundaries in the CG material were limited, which is consistent with the predictions of Fig. 2 for larger grain sizes. This can also be attributed to the decrease in density of $\Sigma 3$ boundaries with increasing grain size due to the detachment of the twin boundaries from the HAGBs resulting in the formation of internal twins.

The grain size distributions for each condition were extracted from the EBSD data. For the determination of the grain size, the parent and twin grains are treated as distinct grains, as represented in Fig. 7. The grain size cumulative probabilities are represented in Fig. 8. Although the parent grain sizes were similar in the baseline $(6.1 \pm 0.2 \ \mu m)$ and GBE material $(5.8 \pm 0.1 \ \mu m)$ in the sub-solvus condition, the higher density of twin boundaries in the GBE sample further divided the grain boundary network, Fig. 5. This resulted in comparatively smaller average grain sizes in the GBE material as compared to the baseline forgings for both FG and CG conditions. In the CG condition, smaller grains were observed in the GBE material from the difference in forging parameters. This resulted in a difference in parent grain size with an average of 49 ± 6 and 33 ± 3 µm in the baseline and GBE CG forgings, respectively. Furthermore, the grain sizes measured in the CG material spanned a significantly larger range (as compared to the FG material) with maximum sizes of up to $\sim 100 \mu m$.



Table 1 Processing conditions for the four variants of RR1000, including isothermal forging condition (temperature and strain rate) and heat treatment. Each heat treatment was performed for 4 h with a controlled cooling rate of 1 °C/s

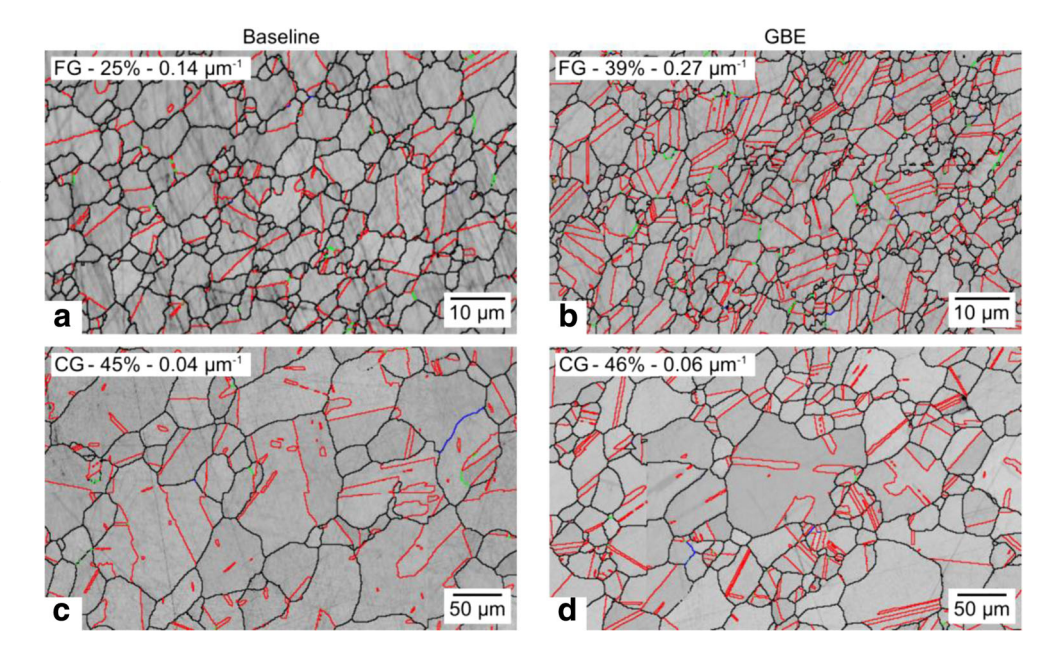
	Conventionally forged (baseline)	Grain boundary engineered (GBE)
Fine grain (FG)	Forged: 1100 °C and 0.003 s ⁻¹	Forged: 1020 °C and 0.05 s ⁻¹
	Sub-solvus annealed: 1115 °C	Sub-solvus annealed: 1115 °C
Coarse grain (CG)	Forged: 1100 °C and 0.003 s^{-1}	Forged: 1020 $^{\circ}$ C and 0.05 s ⁻¹
	Super-solvus annealed: 1170 °C following 1115 °C	Super-solvus annealed: 1170 °C following 1115 °C

Fatigue Simulations

The four lots of materials produced during the forging process were characterized using EBSD and used to create 10 statistically equivalent microstructures (SEMs) for each lot of material using DREAM.3D [67]. All the SEMs used in the current study have at least 150 grains, which makes them large enough to capture not only the microstructural attributes but also the strength properties. The SEMs serve as representative volume elements for the strength properties (e.g., yield stress, hardening behavior, maximum/minimum stress upon cyclic loading in strain control, i.e., the ability to capture the Bauschinger effect), but not necessarily for the minimum fatigue life. By analyzing the result of the 10 SEMs, we captured variability in the fatigue behavior and thereby the fatigue performance. Each SEM was subjected to a single fatigue loading cycle via crystal plasticity to capture the micro-mechanical fields relative to each of microstructure. Based on prior digital image correlation of this material [68], it was observed that the slip bands form during the first loading cycle (and the number of slip bands were constant with respect to number of cycles for this particular loading). One cycle of the crystal plasticity simulation is sufficient to determine the heterogeneities in the stress distributions relative to the microstructural features [40], and the resulting micromechanical fields after one loading cycle are used for fatigue modeling purposes. For each individual SEM, the fatigue model deterministically calculates the fatigue life on a grain-by-grain basis. By using multiple SEMs, thousands of grains can be probed by the fatigue model to obtain their respective fatigue lives and the large amount of data is consolidated to get a fatigue life distribution. The results of the fatigue model are grouped into the CG (super-solvus) and FG (sub-solvus) conditions and plotted as probability of failure in terms of cycles to crack initiation, as shown in Fig. 9. As expected, the sub-solvus annealed RR1000 material displays superior strength properties when compared to the CG variant, which is attributed to the fine grain structure with little variability in grain size distribution. Further, the finer grain structure prevents large PSBs from forming, thereby extending the fatigue life of the material.

For each of the SEM simulations, the critical PSB resulting in crack initiation was further analyzed, such that the PSB length was recorded. Figure 10 displays the inverse relationship between the PSB length and the cycles to crack initiation. As previously stated, the GBE structures have an increased density of twins. Due to the modified isothermal forging process utilizing higher strain rates and lower temperatures, the dislocation mediated deformation results in an increase in stored strain energy within the microstructure that is relieved

Fig. 5 Grain boundary maps of the forged \mathbf{a} , \mathbf{c} baseline and \mathbf{b} , \mathbf{d} GBE billets following annealing resulting in \mathbf{a} , \mathbf{b} FG and \mathbf{c} , \mathbf{d} CG microstructures. The $\Sigma 3$ boundaries are represented in red, $\Sigma 9$ in green, $\Sigma 27$ in blue, and random HAGBs in black. The insets describe the twin density (with respect to surface area) and the twin length fraction, respectively





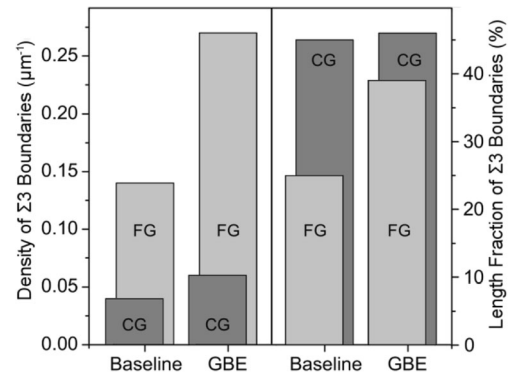


Fig. 6 Density and length fraction of $\Sigma 3$ boundaries in the FG and CG forged baseline and GBE billets. The values are averages over 8 stitched regions which resulted in total scanned areas of $\sim 200 \times 248~\mu m^2$ for the FG condition and $\sim 800 \times 1000~\mu m^2$ for the CG condition

by the formation of annealing twins. As shown in Fig. 7, the annealing twins nucleate and grow across the parent grains during heat treatment, subsequently reducing the effective, overall grain size. Thus, the GBE materials extend the fatigue life in two ways. Firstly, the increased twin density in the grain boundary engineered materials thereby act to reduce the length of the potential PSBs that can form. By having a higher probability of intersecting a twin, the PSB length is limited in the GBE case. Secondly, the GBE material reduces the quantity of LAGBs, and further limits the formation of PSBs across grain clusters (similarly oriented grains connected by LAGBs), which once again reduces the potential PSB length. Therefore, if the material has a large PSB, it is likely to fail quickly, but on the other hand, if a large PSB is inhibited from forming, then the material is likely to fail from smaller PSBs and consequently possess a prolonged life.

Strain Mapping

It is well known that Ni-based superalloys deform with high degrees of heterogeneity [69], manifesting high levels of deformation along slip bands [29]. In order to understand the effects of GBE on this material, it is important to capture the discrete slip bands and their interactions with grain boundaries. To capture material heterogeneity during different stages

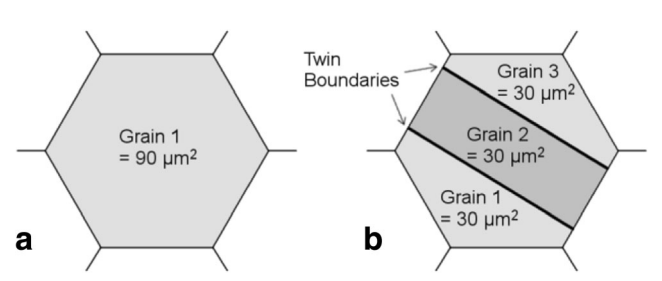


Fig. 7 Schematic view of grain area measurement from ${\bf a}$ parent grain and ${\bf b}$ parent grain with twin



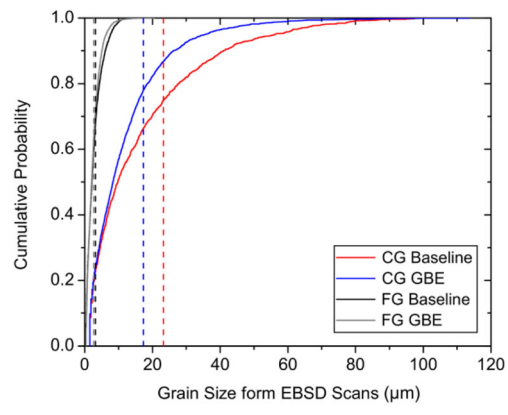


Fig. 8 Grain size cumulative distribution plot for the variants of material produced during this study. The dashed lines represent the average grain size for each case

of deformation, the surface strain is characterized spatially relative to the microstructural features using digital image correlation. Digital image correlation (DIC) is a technique that uses a random surface pattern to track displacements from an initial state. As the sample is deformed, these random surface features are displaced, mirroring the underlying microstructural surface behavior. Image correlation between initial and deformed states yields in-plane surface displacements, which are then integrated into in-plane strain components [70]. In this experiment, the initial state is correlated with deformed states at 1 and 10 fatigue cycles at room temperature. Four different conditions of RR1000 were investigated during this experiment, as previously summarized in Table 1.

Specimen Preparation and Fatigue Testing Conditions

Dog bone specimens were produced via EDM from forged disks of baseline and GBE RR1000. Specimens had gauge sections measuring 10 mm by 3 mm by 1.25 mm thick. A

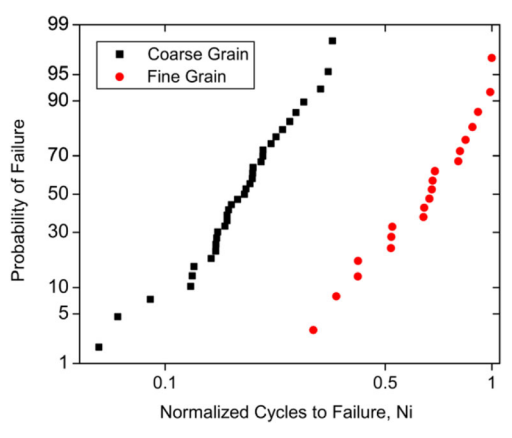


Fig. 9 Fatigue model life predictions for CG and FG RR1000 plotted as the probability of failure, where the cycles to failure are normalized based on the maximum value observed

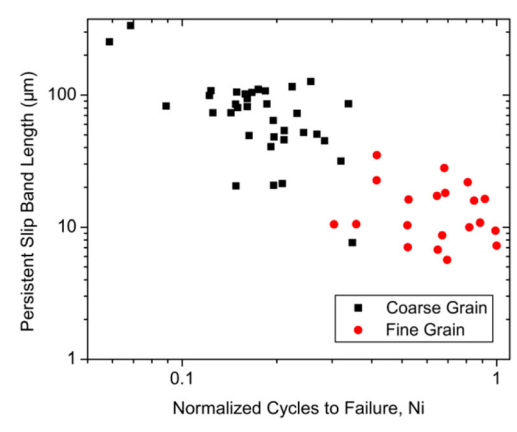


Fig. 10 Fatigue model simulations of the length of the critical PSB resulting in failure plotted against the normalized cycles to failure based on the maximum value observed

cross-section of the forged disk, through the thickness, was taken, and EBSD scans were conducted on these areas, in order to identify and avoid the surface discontinuities produced by the forging process. Forged surfaces were removed, such that a consistent microstructure, specifically the twin density, twin length fraction, and grain size, was present in all specimens. Specimens were prepped via mechanical grinding and polishing. Final polishing was completed with 0.3 and 0.05 μm alumina and colloidal silica, respectively. Fiducial markers were placed in a rectangular array in the middle of each specimen defining the area of interest. The microstructure was characterized via EBSD scans, in order to acquire the spatial crystallographic orientations that were used to reconstruct the spatial position of the grain boundaries.

Specimens were tested with a servo hydraulic MTS machine with an Epsilon model 3442 extensometer attached. The first cycle was composed of monotonic loading to 1% total strain in displacement control in accordance with the ASTM E8 standard for testing aerospace alloys, followed by unloading to a near-zero value of stress in load control and the

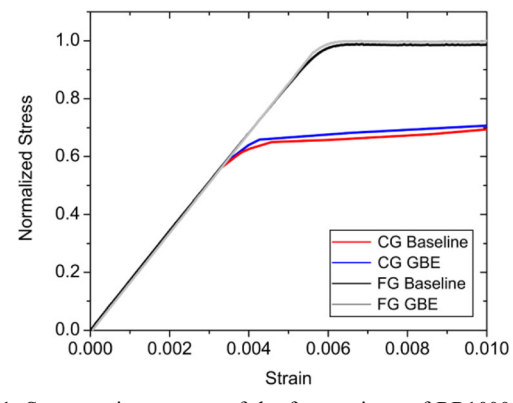


Fig. 11 Stress-strain response of the four variants of RR1000, forged with baseline and GBE parameters and heat treated to the CG and FG conditions. Only the first initial loading cycle to 1% strain is shown, where the stress is normalized based on the maximum value of the FG GBE case

extensometer was subsequently removed. The maximum stress at 1% strain was recorded as depicted in the stress-strain curve for each condition in Fig. 11, and this value of maximum stress was used as the target stress in subsequent cycling. Cycles 2 through 10 were performed in load control with an R-ratio of 0.1 about the measured maximum stress at 1% total strain obtained during the first cycle.

Digital Image Correlation Using Electron Imaging

Images were taken on a Phillips XL40 FEG scanning electron microscope at a resolution of 3872 × 2904 pixels with a working distance of 10 mm. A gold nanoparticle pattern was applied to the specimen's surface following the procedure outlined by Kammers and Daly [71]. The gold nanoparticles provide fine features with sufficient density to enable highresolution DIC analysis, which is capable of identifying individual slip bands, as shown in Fig. 12. Images were also corrected for spatial distortions, and a protocol was followed to minimize drift distortion inherent in electron microscopy described by Sutton et al. [72]. These distortions were removed from the DIC analysis by use of a certified grid at the end of each microscopy session. The calibration grid served as a reference image, which ensured that the reported magnification was consistent for each microscopy session; the full procedure is discussed in detail by Mello et al. [73].

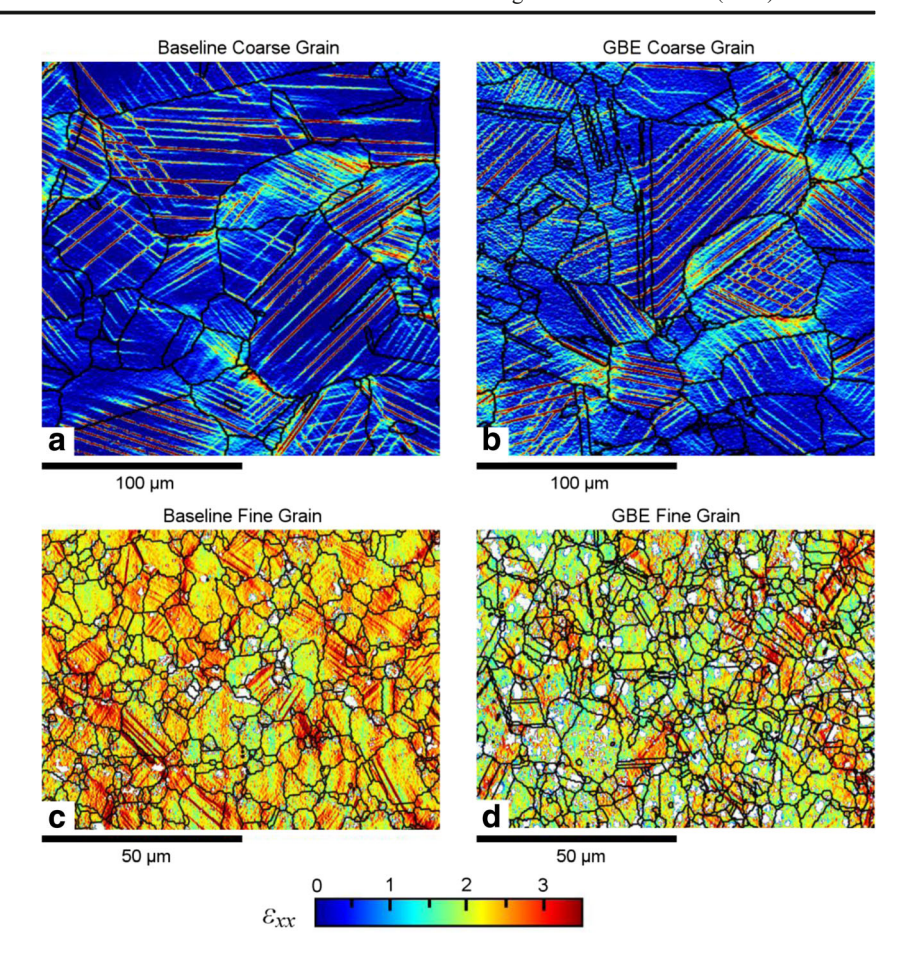
A $100 \times 75 \ \mu\text{m}^2$ area of interest was observed in the fine grain specimens, while a larger area of 200 × 200 µm² was observed in the coarse grain specimens, in order to capture a representative number of grains during the characterization of each specimen. Image correlations were conducted using Correlated Solutions VIC-2DTM. Regions of interest for the analysis of the fine grain material consist of four stitched images; each image was correlated using a subset of $0.42 \times 0.42 \text{ }\mu\text{m}^2$ and a step size of 0.03 μm . The strain maps for the coarse grain samples consist of six stitched images, two wide by three long, and each image was correlated using a subset of $1.34 \times 1.34 \ \mu m^2$ and a step size of $0.06 \ \mu m$. A larger subset was selected for the coarse grain material to capture the discrete slip bands; smaller subsets could not capture the relative large displacements that occurred along slip bands resulting in poor correlations.

Strain Map Results and Discussion

Digital image correlation using images obtained by electron microscopy was conducted on the four aforementioned cases. Strain maps are shown at 10 cycles in Fig. 12. The strain component along the loading direction of the specimen is plotted, ε_{xx} . Strain maps at 10 cycles were selected to demonstrate the role of cyclic hardening, due to the presence of strain accumulation at grain boundaries and along slip bands, but well before diffuse strain



Fig. 12 Scanning electron microscopy-digital image correlation showing (ε_{xx}), loading direction strain, after 10 cycles of a baseline coarse grain, b GBE coarse grain, c baseline fine grain, and d GBE fine grain RR1000. Area imaged for a and b are $200 \times 200 \ \mu m^2$, c and d are $100 \times 75 \ \mu m^2$



images, whereas out-of-plane deformation obscures individual slip bands within grains. The white areas in Fig. 12 correspond to a low confidence value of strain during the digital image correlation process, and thus, the subsequent strain value is not reported in the strain map.

Average strain accumulation in the CG baseline and GBE microstructures in the unloaded state, Fig. 12a, b, are 0.73 and 0.87% after 10 loading cycles, respectively. The baseline structure demonstrates a larger mean distance between slip bands, as a consequence almost all slip activity captured is part of a saturated slip band, where the strain value measured is 3.5% or greater in the loading direction. Meanwhile, the CG GBE structure does contain more strain, Fig. 12b. On average, many of the grains in the CG GBE structure show finer spacing between slip bands, as compared to the CG baseline; this results in strain not localizing on fewer slip bands but rather accommodating the deformation over more slip bands. All slip bands observed were straight, characteristic of shearing γ^\prime precipitates [74] in Ni-based superalloys and indicative of planar slip [75].

The average strain accumulation in the FG microstructures after 10 cycles in the unloaded state is 2.30% and 1.81%, respectively, as shown in Fig. 12c, d. Therefore, the FG GBE structure had less average strain at the end

of 10 cycles when compared to the baseline FG sample, as shown in Table 2. The macroscopic stress-strain curves were similar for the baseline and GBE material in the FG samples. Further, the FG material does have a higher strength in terms of the yield point and stress at 1% strain, compared to the CG material, as explained by the Hall-Petch relationship [76, 77]. Due to the higher stress state, both FG materials, baseline and GBE, showed a higher degree of plasticity when compared to the CG microstructures throughout the experiment.

As previously noted, for the FG microstructures (in both the baseline and GBE cases), the individual slip bands are obscured, such that strain appears as a continuous field. By viewing the strain field, strain manifests along 45°

Table 2 Accumulated average plastic strain states of each RR1000 variant after 1 and 10 fatigue cycles in the unloaded state

Deformation state	1 Cycle	10 Cycles
Baseline fine grain	0.53%	2.30%
GBE fine grain	0.58%	1.81%
Baseline coarse grain	0.54%	0.73%
GBE coarse grain	0.66%	0.87%



macroscopic bands relative to the specimen's loading direction with distinct patterning around microstructural features. Moreover, the higher stress imposed on the FG material results in the activation of multiple slip systems within individual grains, as discussed by Boettner et al. [22] and Kocks and Mecking [78, 79]. These additional slip systems coupled with the smaller slip band spacing explain the inability to resolve slip band in the FG material. Shyam and Milligan [80] investigated the dislocation arrangement in these FG structures via transmission electron microscopy and found that deformation within smaller grains were driven by an isolated movement of dislocations during deformation, not planar slip bands as in coarse grain material. This resulted in highly homogenous deformation, where homogenous deformation was defined as highly decreased spacing between slip bands and activation of multiple slip systems [80].

The individual slip band length was measured in the CG specimens using the software ImageJ [81], which is shown as a cumulative distribution function in Fig. 13. The GBE material has a higher twin boundary fraction, which serves as more internal barriers to slip, inside of each larger parent grain, hindering crack formation. Davidson et al. [52] presented the super-grain theory, in which many grains act in concert to promote crack initiation. Similarly, Sangid et al. [21] demonstrated that large grains and grain clusters connected by LAGBs provided longer slip bands that promoted long range transmission and pile up of dislocations serving as a precursor to crack initiation. Therefore, the increased occurrence of twin boundaries within a larger parent grain allows the one large parent grain to behave like a few smaller grains. Each twin boundary will act as a separate grain boundary, impeding slip continuity across the larger parent grain, therefore acting as the mechanism for GBE-based strengthening and fatigue enhancement of the material.

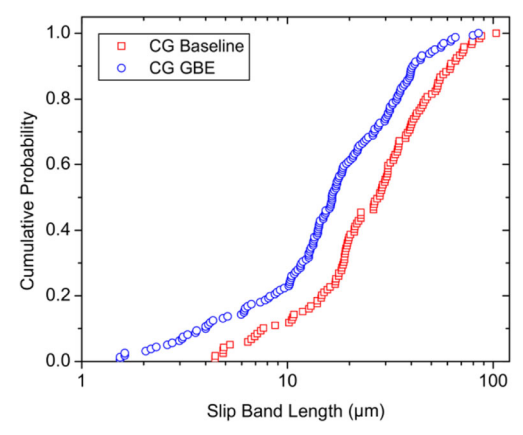


Fig. 13 Cumulative probability distributions of the slip band length in baseline and GBE CG samples as measured from resulting digital image correlation strain maps

Conclusions

An integrated computational materials engineering framework is adopted to design and manufacture a Ni-based superalloy with the objective to tailor the fatigue performance of the resulting forged turbine disks. Significant contributions of this study are summarized as follows:

- 1. An existing fatigue model, based on persistent slip bands (PSBs) [20, 40, 42, 43], is used to identify microstructural features that are beneficial for achieving an enhanced fatigue life. A PSB of longer length is attributed to more stored strain and a higher stress concentration, therefore leading to a shorter fatigue life. Therefore, a small, uniform grain size is preferred without the presence of texture. Further, the grain boundaries play a critical role in the fatigue performance, low-angle GBs, promoting slip transmission and PSB forming across grain clusters, should be avoided. Finally, twin boundaries are beneficial in their role of impeding the length of PSBs that form.
- 2. Conventional GBE approaches are not suited to the processing of Ni-based superalloys for turbine disk applications. Models for the formation and grain size dependence of twin boundaries were used to identify conditions favorable to the improvement of the grain boundary network during isothermal forging. A process map was developed for RR1000, and GBE was achieved using hot deformation parameters that trigger dislocation-based plasticity mechanisms. The residual strain energy stored within the microstructure promoted the formation of twin boundaries during subsequent annealing via SIBM.
- 3. Small-scale forgings of RR1000 were produced using the conventional forging parameters and the modified forging parameters to achieve GBE. Furthermore, two heat treatments, respectively, sub-solvus and super-solvus, were performed to produce fine grain (FG) and coarse grain (CG) microstructures. The density of twin boundaries was almost doubled in the GBE condition compared to the conventionally processed forging, in the FG variants. The CG only showed a modest increase in the density and length fraction of twin boundaries.
- 4. High-resolution DIC was performed on the four variants of RR1000. Each strain map displayed heterogeneous deformation along 45° macroscopic bands relative to the specimen's loading direction and accumulating around microstructural features, especially twin boundaries. Individual strain bands could be readily observed within the strain maps of the CG material. The length of these slip bands was shorter across the GBE material, which, as the fatigue model predicts, is attributed to a longer fatigue life.



Acknowledgements Financial support for this work was provided by the National Science Foundation (grant number CMMI 13-34664 and 13-34998) and Rolls-Royce Corporation. The authors would like to thank Randy Helmink, Robert Goetz, and Eugene Sun of Rolls-Royce Corporation for useful discussions about this work and Saikumar Yeratapally for assistance with the simulations. Martin Detrois is appointed to the U.S. Department of Energy (DOE) Postgraduate Research Program at the National Energy Technology Laboratory administered by the Oak Ridge Institute for Science and Education.

Authors' Contributions ST and MDS conceived the project. The deformation mechanism map, process models for GBE of RR1000, and GBE characterization were performed by MD under the supervision of ST. MH provided technical expertise to produce the small-scale forgings. MDS originated and supervised the fatigue modeling. The DIC strain maps and mechanical behavior analysis were performed by JR under the supervision of MDS. Each author wrote their respective section and the group iterated on the document to converge upon the final form of the manuscript. All authors have read and approved the final manuscript.

Compliance with Ethical Standards

Competing Interests The authors declare that they have no competing interests.

References

- Reed RC (2006) The superalloys: fundamentals and applications. Cambridge University Press, New York. https://doi.org/10.1017/ CBO9780511541285
- Pollock TM, Tin S (2006) Nickel-based superalloys for advanced turbine engines: chemistry, microstructure and properties. J Propuls Power 22(2):361–374. https://doi.org/10.2514/1.18239
- Sims CT, Stoloff NS, Hagel WC (1987) Superalloys II: hightemperature materials for aerospace and industrial power. Wiley, New York
- Durand-Charre M (1998) The microstructure of Superalloys. CRC Press. Boca Raton
- MacLachlan DW, Knowles DM (2001) Modelling and prediction of the stress rupture behaviour of single crystal superalloys. Mater Sci Eng A 302(2):275–285. https://doi.org/10.1016/S0921-5093(00)01829-3
- Ghosh RN, Curtis RV, McLean M (1990) Creep deformation of single crystal superalloys-modelling of the crystallographic anisotropy. Acta Metall Mater 38(10):1977–1992. https://doi.org/10. 1016/0956-7151(90)90309-5
- Furrer D, Fecht H (1999) Ni-based superalloys for turbine discs. JOM 51(1):14–17. https://doi.org/10.1007/s11837-999-0005-y
- Hyde CJ, Sun W, Hyde TH (2011) An investigation of the failure mechanisms in high temperature materials subjected to isothermal and anisothermal fatigue and creep conditions. Procedia Eng 10: 1157–1162. https://doi.org/10.1016/j.proeng.2011.04.192
- Jones J, Whittaker M, Lancaster R, Williams S (2014) Lifting the thermo-mechanical fatigue (TMF) behaviour of the polycrystalline nickel-based superalloy RR1000. MATEC Web Conf 14:19001. https://doi.org/10.1051/matecconf/20141419001
- Schuh CA, Kumar M, King WE (2003) Analysis of grain boundary networks and their evolution during grain boundary engineering. Acta Mater 51:687–700. https://doi.org/10.1016/S1359-6454(02) 00447-0

- Randle V (1996) The role of the coincidence site lattice in grain boundary engineering. The Institute of Materials, London
- Kumar M, King WE, Schwartz AJ (2000) Modifications to the microstructural topology in fcc materials through thermomechanical processing. Acta Mater 48(9):2081–2091. https://doi.org/10.1016/S1359-6454(00)00045-8
- Palumbo G, Aust KT (1992) Special properties of Σ grain boundaries. In: Wolf D, Yip S (eds) Materials interfaces: atomic-level structure and properties. Chapman & Hall, London, pp 190–207
- Kronberg ML, Wilson FH (1949) Secondary recrystallization in copper. AIME Trans
- Olmsted DL (2009) A new class of metrics for the macroscopic crystallographic space of grain boundaries. Acta Mater 57:2793– 2799. https://doi.org/10.1016/j.actamat.2009.02.030
- Olmsted DL, Foiles SM, Holm EA (2009) Survey of computed grain boundary properties in face-centered cubic metals: I. Grain boundary energy. Acta Mater 57:3694–3703. https://doi.org/10. 1016/j.actamat.2009.04.007
- Randle V (1999) Mechanism of twinning-induced grain boundary engineering in low stacking-fault energy materials. Acta Metall 47: 4187–4196. https://doi.org/10.1016/S1359-6454(99)00277-3
- Lu K, Lu L, Suresh S (2009) Strengthening materials by engineering coherent internal boundaries at the nanoscale. Science 324(5925):349–352. https://doi.org/10.1126/science.1159610
- Gao Y, Ritchie RO, Kumar M, Nalla RK (2005) High-cycle fatigue of nickel-based superalloy ME3 at ambient and elevated temperatures: role of grain-boundary engineering. Metall Mater Trans A 36(12):3325–3333. https://doi.org/10.1007/s11661-005-0007-5
- Gao Y, Stölken JS, Kumar M, Ritchie RO (2007) High-cycle fatigue of nickel-base superalloy René 104 (ME3): interaction of microstructurally small cracks with grain boundaries of known character. Acta Mater 55(9):3155–3167. https://doi.org/10.1016/j.actamat.2007.01.033
- Sangid MD, Maier HJ, Sehitoglu H (2011) The role of grain boundaries on fatigue crack initiation—an energy approach. Int J Plast 27(5):801–821. https://doi.org/10.1016/j.ijplas.2010.09.009
- Boettner RC, McEvily AJ Jr, Liu YC (1964) On the formation of fatigue cracks at twin boundaries. Philos Mag 10(103):95–106. https://doi.org/10.1080/14786436408224210
- Thompson A (1972) The influence of grain and tlin boundaries in fatigue cracking. Acta Metall 20(9):1085–1094. https://doi.org/10. 1016/0001-6160(72)90172-1
- Qu S, Zhang P, Wu SD, Zang QS, Zhang ZF (2008) Twin boundaries: strong or weak? Scr Mater 59(10):1131–1134. https://doi.org/10.1016/j.scriptamat.2008.07.037
- Abuzaid W, Sehitoglu H, Lambros J (2013) Plastic strain localization and fatigue micro-crack formation in Hastelloy X. Mater Sci Eng A 561:507–519. https://doi.org/10.1016/j.msea.2012.10.072
- Blochwitz C, Tirschler W (2005) Twin boundaries as crack nucleation sites. Cryst Res Technol 40(1–2):32–41. https://doi.org/10. 1002/crat.200410305
- 27. Hashimoto S, Ikehata H, Kato A, Kato H, Kaneko Y (1999) Fatigue crack nucleation at $\Sigma 3$ (1 1 2) boundary in a ferritic stainless steel. Interface Sci 7(2):159–171. https://doi.org/10.1023/A: 1008739820261
- Miao J, Pollock TM, Jones JW (2009) Crystallographic fatigue crack initiation in nickel-based superalloy René 88DT at elevated temperature. Acta Mater 57(20):5964–5974. https://doi.org/10. 1016/j.actamat.2009.08.022
- Stinville JC, Vanderesse N, Bridier F, Bocher P, Pollock TM (2015) High resolution mapping of strain localization near twin boundaries in a nickel-based superalloy. Acta Mater 98:29–42. https://doi.org/ 10.1016/j.actamat.2015.07.016



- Alam Z, Eastman D, Weber G, Ghosh S, Hemker K (2016) Microstructural aspects of fatigue crack initiation and short crack growth in René 88DT. In: Hardy M, Huron E, Glatzel U, Griffin B, Lewis B, Rae C, Seetharaman V, Tin S (eds) Superalloys 2016: proceedings of the 13th international symposium of Superalloys. Wiley, Hoboken, pp 561–568. https://doi.org/10.1002/ 9781119075646.ch60
- Peralta P, Llanes L, Bassani J, Laird C (1994) Deformation from twin-boundary stresses and the role of texture: application to fatigue. Philos Mag A 70(1):219–232. https://doi.org/10.1080/ 01418619408242547
- Neumann P (1999) Analytical solution for the incompatibility stresses at twin boundaries in cubic crystals. In: Wu XR (ed) Proceedings of the 7th International Fatigue Conference (FATIGUE'99). 1:4
- Shenoy M, Tjiptowidjojo Y, McDowell D (2008) Microstructuresensitive modeling of polycrystalline IN 100. Int J Plast 24:1694– 1730. https://doi.org/10.1016/j.ijplas.2008.01.001
- Przybyla CP, McDowell DL (2010) Microstructure-sensitive extreme value probabilities for high cycle fatigue of Ni-base superalloy IN100. Int J Plast 26:372–394. https://doi.org/10.1016/j.ijplas. 2009.08.001
- Castelluccio GM, McDowell DL (2013) Effect of annealing twins on crack initiation under high cycle fatigue conditions. J Mater Sci 48(6):2376–2387. https://doi.org/10.1007/s10853-012-7021-y
- Keshavarz S, Ghosh S (2015) Hierarchical crystal plasticity FE model for nickel-based superalloys: sub-grain microstructures to polycrystalline aggregates. Int J Solids Struct 55:17–31. https:// doi.org/10.1016/j.ijsolstr.2014.03.037
- Zhang T, Jiang J, Britton B, Shollock B, Dunne F (2015) Crack nucleation using combined crystal plasticity modelling, highresolution digital image correlation and high-resolution electron backscatter diffraction in a superalloy containing non-metallic inclusions under fatigue. Proc R Soc A 472:0792. https://doi.org/10. 1098/rspa.2015.0792
- Wan VVC, MacLachlan DW, Dunne FPE (2014) A stored energy criterion for fatigue crack nucleation in polycrystals. Int J Fatigue 68:90–102. https://doi.org/10.1016/j.ijfatigue.2014.06.001
- Cerrone A, Stein C, Pokharel R, Hefferan C, Lind J, Tucker H, Suter R, Rollett A, Ingraffea A (2015) Implementation and verification of a microstructure-based capability for modeling microcrack nucleation in LSHR at room temperature. Model Simul Mater Sci Eng 23(3):035006. https://doi.org/10.1088/0965-0393/23/3/035006
- Yeratapally SR, Glavicic MG, Hardy M, Sangid MD (2016) Microstructure based fatigue life prediction framework for polycrystalline nickel-base superalloys with emphasis on the role played by twin boundaries in crack initiation. Acta Mater 107:152–167. https://doi.org/10.1016/j.actamat.2016.01.038
- Tanaka K, Mura T (1981) A dislocation model for fatigue crack initiation. J Appl Mech 48:97–103. https://doi.org/10.1115/1. 3157599
- Sangid MD, Maier HJ, Sehitoglu H (2011) A physically based fatigue model for prediction of crack initiation from persistent slip bands in polycrystals. Acta Mater 59:328–341. https://doi.org/10. 1016/j.actamat.2010.09.036
- Sangid MD, Maier HJ, Sehitoglu H (2011) An energy-based microstructure model to account for fatigue scatter in polycrystals. J Mech Phys Solids 59:595–609. https://doi.org/10.1016/j.jmps. 2010.12.014
- Armstrong PJ, Frederick CO (1966) A mathematical representation of the multiaxial Bauschinger effect. Report RD/B/N, 731, Central Electricity Generating Board, Berkeley, UK

- Schouwenaars R, Seefeldt M, Van Houtte P (2010) The stress field of an array of parallel dislocation pile-ups: implications for grain boundary hardening and excess dislocation distributions. Acta Mater 58: 4344–4353. https://doi.org/10.1016/j.actamat.2010.04.026
- Taylor GI (1934) The mechanism of plastic deformation of crystals.
 Proc Roy Soc 145:362–387. https://doi.org/10.1098/rspa.1934.0106
- Sangid MD, Ezaz T, Sehitoglu H, Robertson IM (2011) Energy of slip transmission and nucleation at grain boundaries. Acta Mater 59: 283–296. https://doi.org/10.1016/j.actamat.2010.09.032
- Essmann U, Gosele U, Mughrabi H (1981) A model of extrusions and intrusions in fatigued metals. I. Point-defect production and the growth of extrusions. Philos Mag A 44:405–426. https://doi.org/10. 1080/01418618108239541
- Differt K, Essmann U, Mughrabi H (1986) A model of extrusions and intrusions in fatigued metals. II. Surface roughening by random irreversible slip. Philos Mag A 54:237–258. https://doi.org/10. 1080/01418618608242897
- Stroh AN (1957) A theory of the fracture of metals. Adv Phys 6: 418–465. https://doi.org/10.1080/00018735700101406
- Zhang ZF, Wang ZG (2003) Dependence of intergranular fatigue cracking on the interactions of persistent slip bands with grain boundaries. Acta Mater 51:347–364. https://doi.org/10.1016/ S1359-6454(02)00399-3
- Davidson DL, Tryon RG, Oja M, Matthews R, Ravi Chandran KS (2007) Fatigue crack initiation in WASPALOY at 20 °C. Metall Mater Trans A 38A:2214–2225. https://doi.org/10.1007/s11661-007-9178-6
- Yeratapally SR, Glavicic MG, Argyrakis C, Sangid MD (2017) Bayesian uncertainty quantification and propagation for validation of a microstructure sensitive model for prediction of fatigue crack initiation. Reliab Eng Syst Saf 164:110–123. https://doi.org/10. 1016/j.ress.2017.03.006
- Sangid MD, Sehitoglu H, Maier HJ, Niendorf T (2010) Grain boundary characterization and energetics of superalloys. Mater Sci Eng A 527:7115–7125. https://doi.org/10.1016/j.msea.2010. 07.062
- Palumbo G, Lehockey EM, Lin P (1998) Applications for grain boundary engineered materials. JOM 50:40–43. https://doi.org/10. 1007/s11837-998-0248-z
- Watanabe T (1984) An approach to grain boundary design for strong and ductile polycrystals. Res Mechanica 11(1):47–84
- Randle V (2004) Twinning-related grain boundary engineering. Acta Mater 52:4067–4081. https://doi.org/10.1016/j.actamat.2004. 05.031
- Detrois M, Rotella J, Goetz RL, Helmink RC, Tin S (2015) Grain boundary engineering of powder processed Ni-base superalloy RR1000: influence of the deformation parameters. Mater Sci Eng A 627:95–105. https://doi.org/10.1016/j.msea.2014.12.112
- Detrois M, Goetz RL, Helmink RC, Tin S (2015) Modeling the effect of thermal-mechanical processing parameters on the density and length fraction of twin boundaries in Ni-base superalloy RR1000. Mater Sci Eng A 647:157–162. https://doi.org/10.1016/ j.msea.2015.09.022
- Detrois M, Goetz RL, Helmink RC, Tin S (2016) The role of texturing and recrystallization during grain boundary engineering of Ni-based superalloy RR1000. J Mater Sci 51(11):5122–5138. https://doi.org/10.1007/s10853-016-9815-9
- Detrois M, McCarley J, Antonov S, Helmink RC, Goetz RL, Tin S (2016) Comparative study of high-temperature grain boundary engineering of two powder-processed low stacking-fault energy Nibase superalloys. Mater High Temp 33:310–317. https://doi.org/10.1080/09603409.2016.1155689



- 62. Detrois M, Rotella R, Goetz RL, Helmink RC, Tin S (2016) The influence of the starting grain size during high-temperature grain boundary engineering of Ni-Base Superalloy RR1000. In: Hardy M, Huron E, Glatzel U, Griffin B, Lewis B, Rae C, Seetharaman V, Tin S (eds) Superalloys 2016: proceedings of the 13th international symposium of Superalloys. Wiley, Hoboken, pp 459–468. https://doi.org/10.1002/9781119075646.ch49
- Pande CS, Imam MA, Rath BB (1990) Study of annealing twins in FCC metals and alloys. Metall Mater Trans A 21:2891–2896. https://doi.org/10.1007/BF02647209
- Li Q, Cahoon JR, Richards NL (2009) Effects of thermomechanical processing parameters on the special boundary configurations of commercially pure nickel. Mater Sci Eng A 527:263–271. https://doi.org/10.1016/j.msea.2009.07.064
- Cahoon JR, Li Q, Richards NL (2009) Microstructural and processing factors influencing the formation of annealing twins. Mater Sci Eng A 526:56–61. https://doi.org/10.1016/j.msea.2009.07.021
- Collins DM, Conduit BD, Stone HJ, Hardy MC, Conduit GJ, Mitchell RJ (2013) Grain growth behaviour during near-γ' solvus thermal exposures in a polycrystalline nickel-base superalloy. Acta Mater 61:3378–3391. https://doi.org/10.1016/j.actamat.2013.02.028
- Groeber MA, Jackson MA (2014) DREAM.3D: a digital representation environment for the analysis of microstructure in 3D. Integr Mater Manuf Innov 3:1–17. https://doi.org/10.1186/2193-9772-3-5
- Mello AW, Nicolas A, Sangid MD (2017) Fatigue strain mapping via digital image correlation for Ni-based superalloys: the role of thermal activation on cube slip. Mater Sci Eng A 695:332–341. https://doi.org/10.1016/j.msea.2017.04.002
- Abuzaid WZ, Sangid MD, Carroll JD et al (2012) Slip transfer and plastic strain accumulation across grain boundaries in Hastelloy X. J Mech Phys Solids 60:1201–1220. https://doi.org/10.1016/j.jmps. 2012.02.001
- Chu TC, Ranson WF, Sutton MA, Peters WH (1985) Applications of digital image correlation techniques to experimental mechanics. Exp Mech 25:232–244. https://doi.org/10.1007/BF02325092

- Kammers AD, Daly S (2013) Self-assembled nanoparticle surface patterning for improved digital image correlation in a scanning electron microscope. Exp Mech 53:1333–1341. https://doi.org/10. 1007/s11340-013-9734-5
- Sutton MA, Li N, Garcia D et al (2006) Metrology in a scanning electron microscope: theoretical developments and experimental validation. Meas Sci Technol 17:2613. https://doi.org/10.1088/ 0957-0233/17/10/012
- Mello A, Book T, Nicolas A et al (2017) Distortion correction protocol for digital image correlation within a scan electron microscope: emphasis on long duration and ex-situ experiments. Exp. Mech 57:1395–1409. https://doi.org/10.1007/s11340-017-0303-1
- Stoltz RE, Pineau AG, Materiaux C (1978) Dislocation-precipitate interaction. 34:275–284
- Ho HS, Risbet M, Feaugas X (2015) On the unified view of the contribution of plastic strain to cyclic crack initiation: impact of the progressive transformation of shear bands to persistent slip bands. Acta Mater 85:155–167. https://doi.org/10.1016/j.actamat.2014.11.020
- Hall EO (1951) The deformation and ageing of mild steel: III discussion of results. Proc Phys Soc Sect B 64:747–753. https://doi.org/10.1088/0370-1301/64/9/303
- Petch NJ (1953) The cleavage strength of polycrystals. J Iron Steel Inst 174
- Kocks UF (1970) The relation between polycrystal deformation and single-crystal deformation. Metall Mater Trans 1:1121–1143. https://doi.org/10.1007/BF02900224
- Mecking H (1981) Deformation of polycrystals: mechanisms and microstuctures. p 73
- Shyam A, Milligan WW (2004) Effects of deformation behavior on fatigue fracture surface morphology in a nickel-base superalloy. Acta Mater 52:1503–1513. https://doi.org/10.1016/j.actamat.2003. 11.032
- Schneider CA, Rasband WS, Eliceiri KW (2012) NIH image to ImageJ: 25 years of image analysis. Nat Methods 9:671–675. https://doi.org/10.1038/nmeth.2089

